

## Supplementary Information

### **Bioinspired Foam with Large 3D-Macropore for Efficient Solar Steam Generation**

*Wentao Zhang,<sup>‡a</sup> Wenxin Zhu,<sup>‡a</sup> Shuo Shi,<sup>a</sup> Na Hu,<sup>b</sup> Yourui Suo,<sup>b</sup> Jianlong Wang<sup>\*a</sup>*

<sup>a</sup> College of Food Science and Engineering, Northwest A&F University, Yangling, 712100, Shaanxi, P. R. China.

<sup>b</sup> Qinghai Key Laboratory of Qinghai-Tibet Plateau Biological Resources, Northwest Institute of Plateau Biology, Chinese Academy of Sciences, Xining, 810008, Qinghai, P. R. China.

\* Corresponding author: wanglong79@yahoo.com

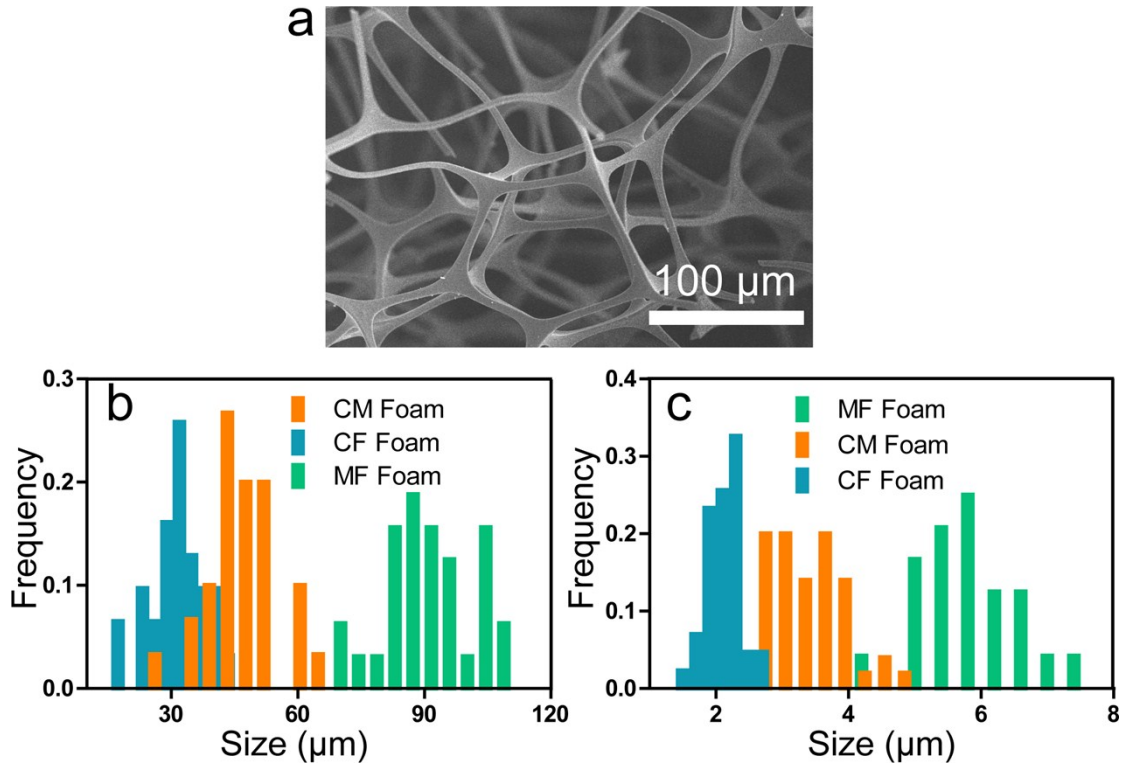


**Fig. S1** (a) The SEM image of MF foam. (b) The distribution of 3D network diameter of MF (90.42 μm), CF (35.53 μm) and CM (47.86 μm) foams. (c) The distribution of carbon skeleton thickness of MF (5.78 μm), CF (2.12 μm) and CM (3.37 μm) foams.

The pore sizes and the network diameters of various foams were counted. As shown in Fig. S1b, without ATTM loading, the network diameter of the resultant foam changes significantly by a factor of  $\sim 2.5$ , while foam with ATTM loading shows a smaller diameter decrease by a factor of  $\sim 1.9$ . Meanwhile, compared with MF foam, the skeleton thickness shrinks by  $\sim 2.7$  times for CF foam and only  $\sim 1.7$  times for CM foam. Hence, with the loading of in-situ crystallized MoS<sub>2</sub> nanoparticles, the skeleton shrinkage of carbon foam can be efficiently inhibited, giving rise to bigger sized foam with bigger 3D macropores than the one annealed alone.

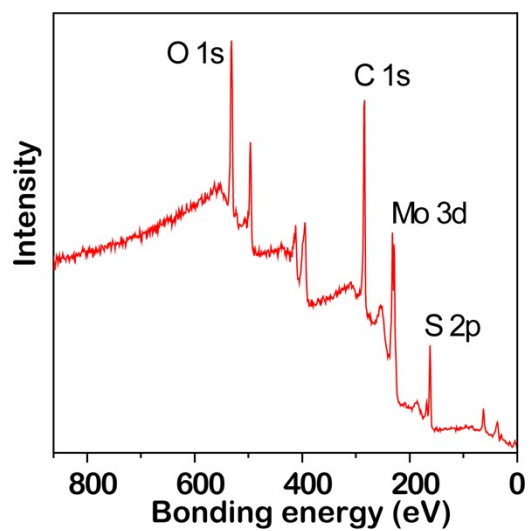


**Fig. S2.** XPS survey data of CM foam.

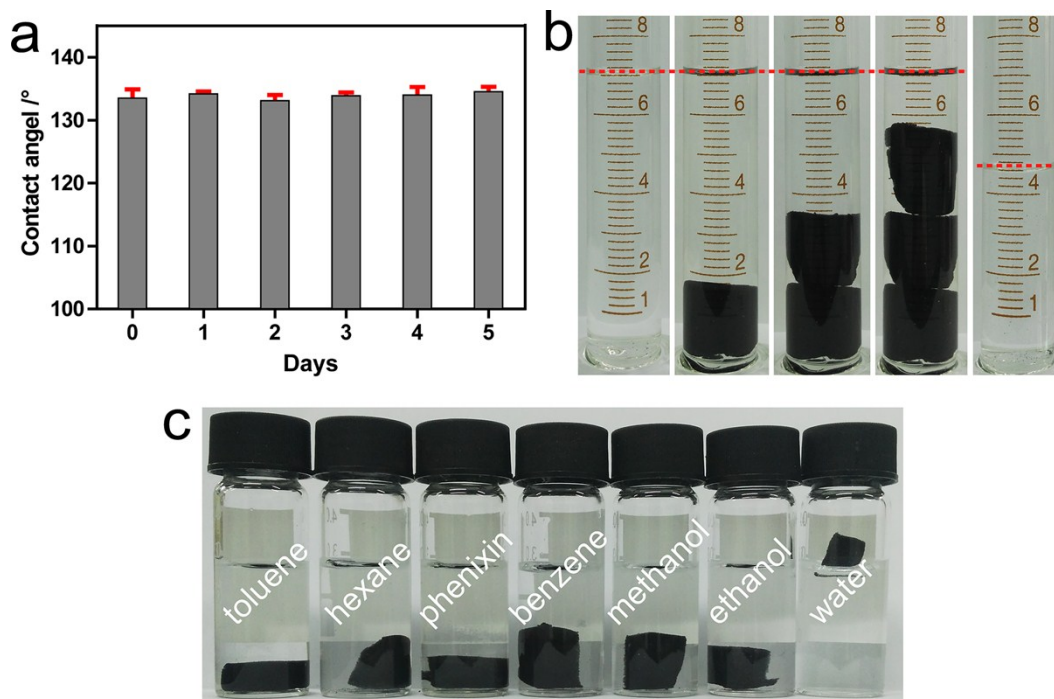


**Fig. S3.** (a) Static water contact angles of the CM foam after immersing in ethanol for different days. (b) Demonstration of big porosity of CM foam by gradually soaking 3 pieces of foam into 7 mL ethanol. (c) Digital images of CM foams immersed in various solvents.

In this work, the solvent used for porosity determination was ethanol. Therefore, the inertness of the foams was tested by putting the foams in ethanol for 5 days. Then, the foams were dried in a vacuum oven at 40 °C for 3 h, cooled down to room temperature, and characterized with contact angle measurements.<sup>1</sup> As shown in Fig. S3a, water contact angles of the foams after being immersed in ethanol for different days are all around 133°, indicating that the CM foam is stable and can keep their hydrophobicity in ethanol. Besides, carbon foam has been widely applied for organic solvent adsorption, including ethanol, methanol, toluene, benzene, vacuum oil, decane, acetone and so on.<sup>2</sup> Moreover, MoS<sub>2</sub> is insoluble in ethanol and hardly dispersed in ethanol even under sonication.<sup>3,4</sup> Therefore, CM foam is inert in ethanol, ensuring the feasibility of fluid saturation technique to estimate the porosities of foams in this work.

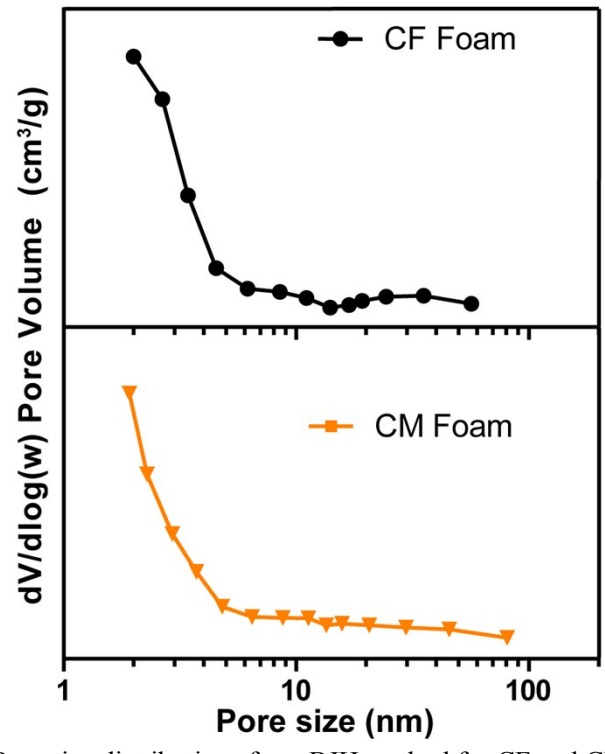


Fig. S4 Pore size distributions from BJH method for CF and CM foams.

### ***Oil/Water Separation Performance of CM Foam***

As shown in Fig. S5, CM foam can immediately adsorb the hexane floated on the surface of water and still float on water. With the assistance of tweezers, the foam can be immersed beneath the surface of water and then serves as hydrophobicity-selective adsorbent for the removal of underwater phenixin droplet from water. Meanwhile, silver film clearly arises on the surface of CM foam, which is attributed to the formation of air/water interface around the CM foam, implying the remarkable hydrophobicity of CM foam.<sup>5</sup> These results directly demonstrate the well potential of CM foam for oil/water separation. The separation performance was evaluated by using CM foam as filter and a mixture of 30 mL phenixin/water (V/V: 2/1) as test solution. During the phenixin/water separation process, phenixin (the transparent part) can continuously and rapidly penetrate the CM foam filter while the water phase (orange color) was retained above the filter (Fig. S5b). Calculated by a previous reported method (Equation 3),<sup>6</sup> the separation ratio of oil phase is higher than 99% although ~30  $\mu$ L phenixin is held beneath the filter due to the difference in pressure intensity (Fig. S6), demonstrating the high separation performance of CM foam. Interestingly, over time after the separation process till 5 h, the water phase still holds above the CM foam filter without any leakage (Fig. S6). Therefore, as a flexible and hydrophobic material, CM foam shows well potential as sealant to temporarily block the leakage of aqueous solutions.<sup>7</sup>

$$R(\%) = \frac{(V_c + V_f)}{V_o} \cdot 100 \quad (3)$$

where  $V_o$  and  $V_c$  are the volume of the original oil and the collected oil, respectively, and  $V_f$  is the volume of absorbed oil in foams collected by squeezing.

The oil absorption capacity ( $Q$ ) of CM foam was then measured. Then absorption capacity was calculated by using the equation of  $Q = (g_t - g_0)/g_0$ , where  $g_0$  and  $g_t$  represent the weight of CM foams before and after oil absorption, respectively. The absorption capacity of CM foam for the tested solvents is shown in Fig. S5c. It reveals that the CM foam exhibits excellent absorption capacity in the range 65.3–159.5 times depending on the type of the absorbed liquids. The oil-absorption capacity of CM foam is higher than other carbonized melamine foam based composites, polymer aerogels, and graphene-based or carbon monolith (Table S1), indicating that the CM foam with shrinkage-inhibited skeleton is an excellent adsorbent for oil/water separation.

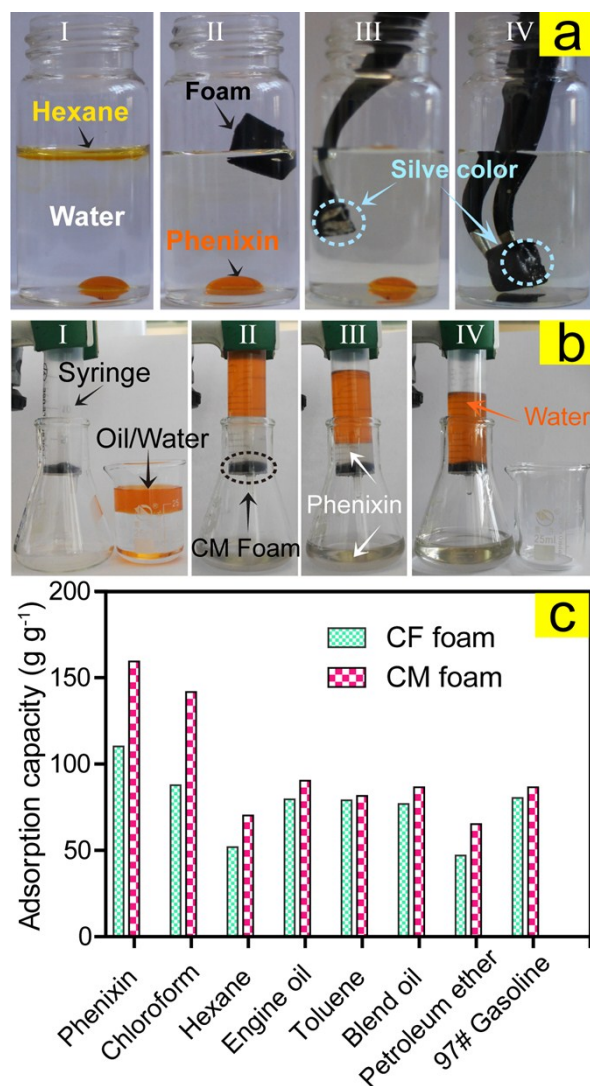


**Fig. S5.** (a) Above- and under-water adsorption of hexane and phenixin (dyed by methyl red) by a piece of CM foam. (b) Photos of oil/water separation process by using CM foam as the filter, and the water was stained by sunset yellow. (c) The adsorption capacity of CF and CM foams toward various organic solvents and oils.

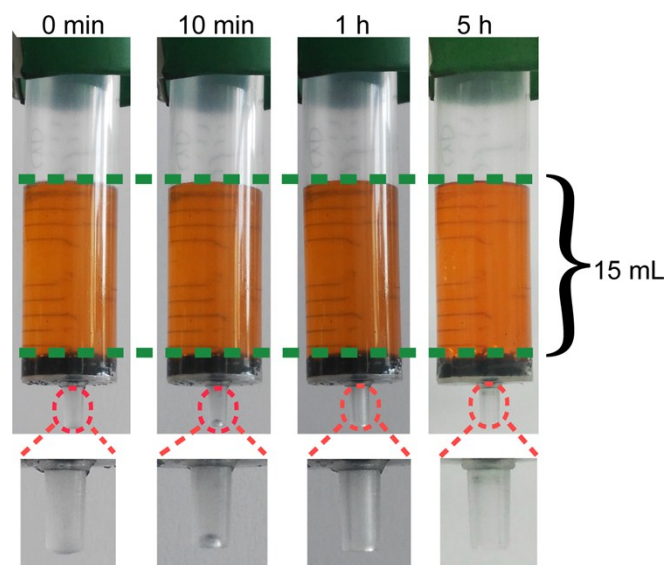


**Fig. S6.** Digital images dyed water in syringe at different time after the oil/water separation process, showing the volatilization of residual phenixin in syringe needle, while no water leakage happens.

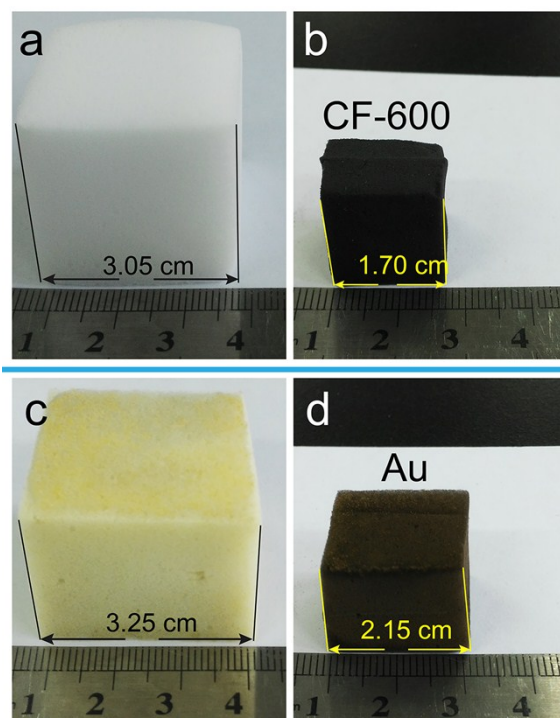


**Fig. S7.** Optical images showing shape transformation of MF foam and  $\text{HAuCl}_4$  loaded MF foam before (a,c) and after (b,d) calcination at 600 °C for 2 h in argon atmosphere. The volume of CF-600 changes significantly by a factor of  $\sim 5.78$  after annealing, while foam with  $\text{HAuCl}_4$  shows a smaller volume decrease by a factor of  $\sim 3.45$ .

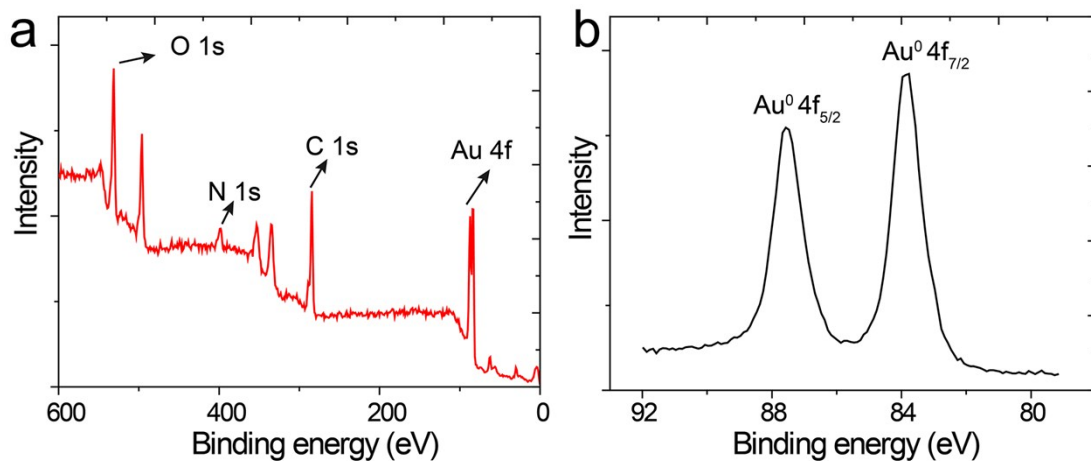


**Fig. S8.** (a) XPS survey data of HAuCl<sub>4</sub>/MF foam transformed hybrid foam, and (b) high-resolution XPS spectrum of Au element.

Fig. S8 shows the spectrum of Au 4f of Au loaded foam. It can be observed that there are two peaks centered at 87.2 eV and 83.7 eV, which are ascribed to the peaks of Au 4f<sub>5/2</sub> and Au 4f<sub>7/2</sub>, respectively, indicating the formation of elemental Au NPs.<sup>8</sup>

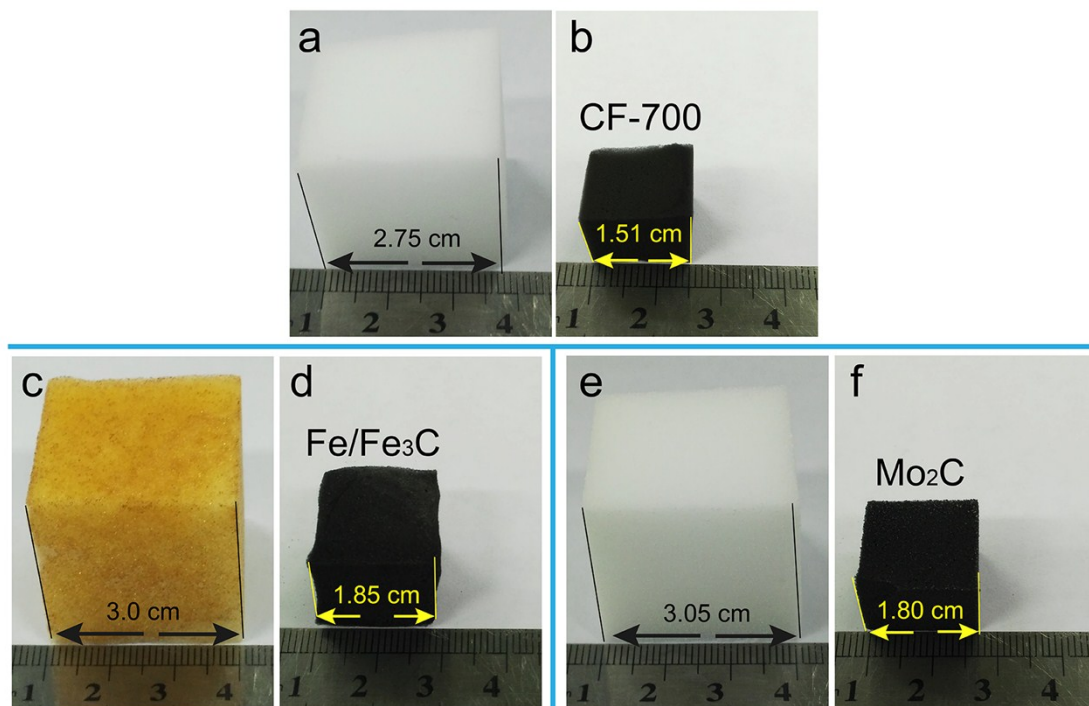


**Fig. S9.** Optical images showing shape transformation of (a) MF foam, (c)  $\text{Fe}(\text{NO}_3)_2$  and (e)  $(\text{NH}_4)_6\text{Mo}_7\text{O}_{24}$  loaded MF foams before and after (b,d,f) calcination at 700 °C for 2 h in argon atmosphere. The volume of CF-700 changes significantly by a factor of  $\sim 6.04$  after annealing, while foam with  $\text{Fe}(\text{NO}_3)_2$  shows a smaller volume decrease by a factor of  $\sim 4.26$ , and  $\sim 4.86$  for  $(\text{NH}_4)_6\text{Mo}_7\text{O}_{24}$  loaded foam.

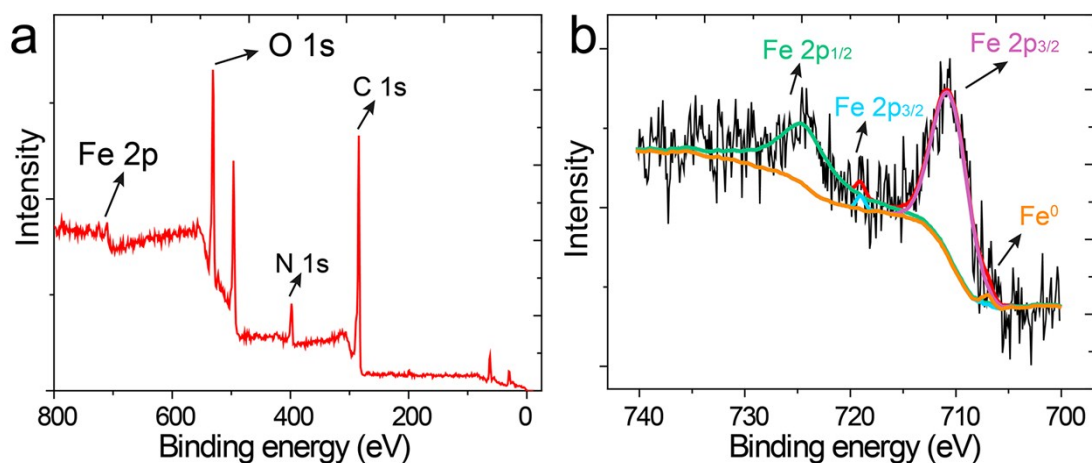


**Fig. S10.** (a) XPS survey data of  $\text{Fe}(\text{NO}_3)_2/\text{MF}$  foam transformed hybrid foam, and (b) high-resolution XPS spectrum of Fe element, indicating the formation of  $\text{Fe}/\text{Fe}_3\text{C}$ .

In terms of the Fe 2p spectrum, the peaks at 711, 719, and 724 eV are assigned to  $\text{Fe } 2p_{3/2}$ , shake-up satellite  $\text{Fe } 2p_{3/2}$  and  $\text{Fe } 2p_{1/2}$  of  $\text{Fe}^{3+}$ , respectively. The signal at 707 eV belongs to  $\text{Fe}^0$ . These results imply the coexistence of Fe and  $\text{Fe}_3\text{C}$  in the hybrid foam.<sup>9</sup>

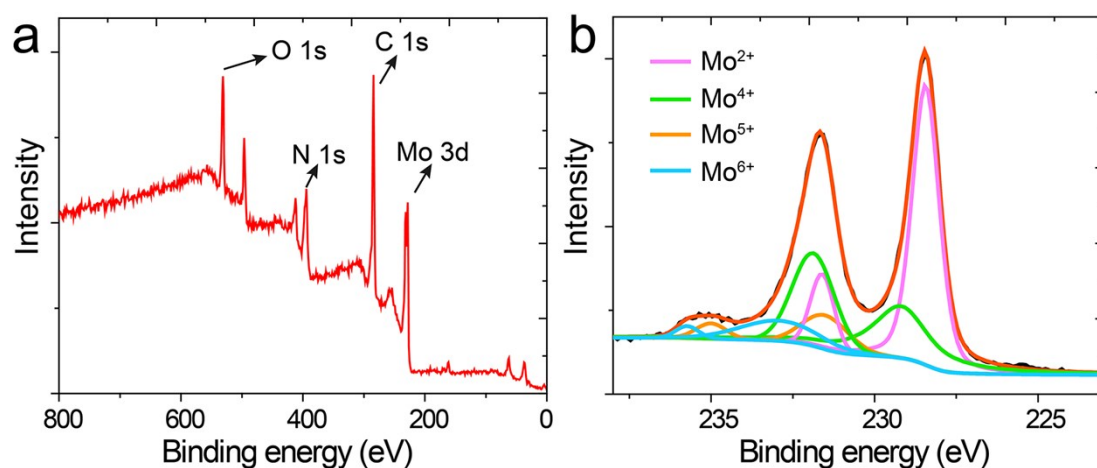


**Fig. S11.** (a) XPS survey data of  $(\text{NH}_4)_6\text{Mo}_7\text{O}_{24}$ /MF foam transformed hybrid foam, and (b) high-resolution XPS spectrum of Mo element, indicating the formation of  $\text{Mo}_2\text{C}$ .

The peak located at binding energy 228.4 and 231.6 eV is assigned to  $\text{Mo}^{2+}$  ( $3d_{5/2}$  and  $3d_{3/2}$ , respectively), consistent with the carbonic phase. Other  $3d_{5/2}$  and  $3d_{3/2}$  binding energies 229.2 and 231.9 eV for  $\text{Mo}^{4+}$ , 231.5 and 235.0 eV for  $\text{Mo}^{5+}$ , 232.9 and 235.7 eV for  $\text{Mo}^{6+}$  are also observed. And no metallic Mo is detected. The ratio of surface  $\text{Mo}^{2+}$  to the oxidation states ( $\text{Mo}^{4+}$ ,  $\text{Mo}^{5+}$  and  $\text{Mo}^{6+}$ ) is about 2.71. The presence of mixed oxidation states of  $\text{Mo}^{4+}$ ,  $\text{Mo}^{5+}$  and  $\text{Mo}^{6+}$  arising from superficial oxidation of  $\text{Mo}_2\text{C}$  due to air contact further indicates the formation of  $\text{Mo}_2\text{C}$ .<sup>10</sup>

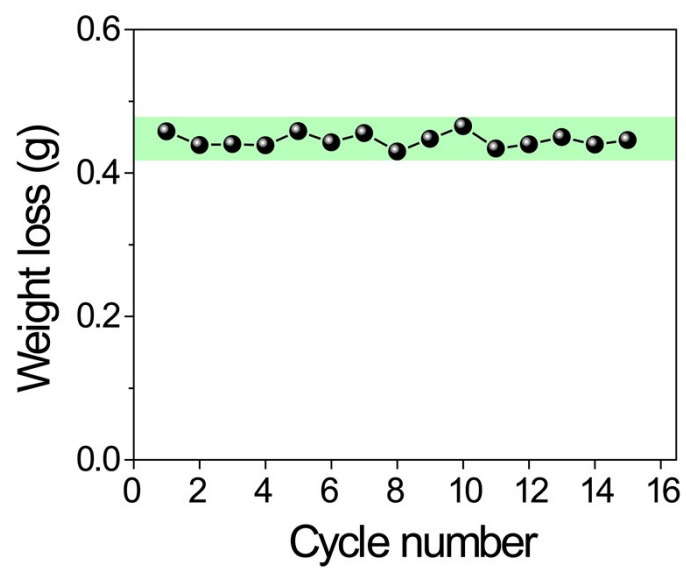


**Fig. S12.** Weight loss through water evaporation after irradiation of the CM foam for 1 h over 15 cycles showing the reusability of CM foam.

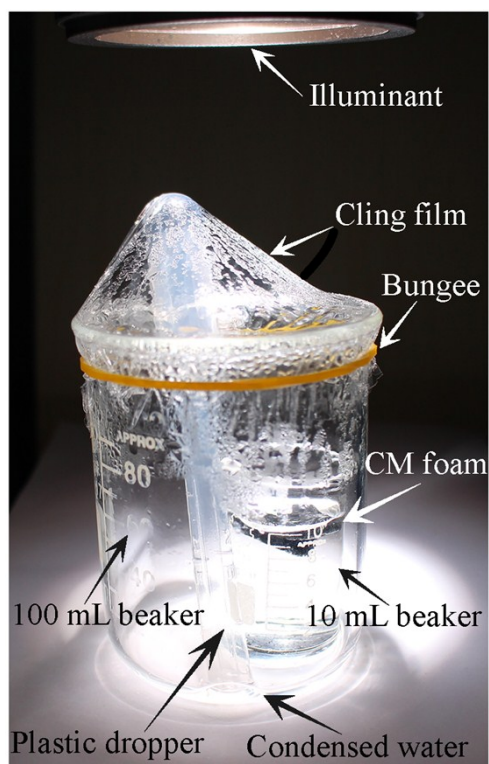


**Fig. S13.** Digital photograph of the point-of-use device for direct and all-in-one solar distillation.

**Table S1** Porous structure parameters of CF and CM foams.

Samples	BET surface area (m <sup>2</sup> g <sup>-1</sup> )	Pore volume (cm <sup>3</sup> g <sup>-1</sup> )	Average pore size (nm)
CF foam	40.3	0.04	3.1
CM foam	322.7	0.15	3.4

**Table S2.** Comparison of adsorption capacities of various adsorbents for oil adsorption.

Adsorbent	Adsorption capacity (times)	Ref.
Chlorotrimethylsilane-modified carbon foam	71–158	11
ZIF-8/CN foam	55–136	2
Resol-melamine derived carbon monolith	0.89–2.03	12
Magnetic melamine foam	60–160	13
Dopamine-melamine foam	60–130	14
Monolithic conjugated microporous polymer aerogels	20–53	15
Magnetic PU-based graphene foam	9–27	16
NRC Aerogels	6–14	17
Carbon soot	25–80	18
Sponge@HFGO@ZIF-8	1.5–6	19
<b>CM foam</b>	<b>65.3–159.5</b>	<b>This work</b>

**Table S3.** Comparison of solar steam generation performances of various hydrophobic self-floating materials.

Photothermal agent	Solar intensity (kW m <sup>-2</sup> )	Evaporation rate (kg m <sup>-2</sup> h <sup>-1</sup> )	Conversion efficiency (%)	Ref.
TiO <sub>x</sub> coated meshes-3	1	0.7936	49.82	20
TiO <sub>x</sub> coated meshes-4	1	0.8012	50.30	20
Al NP/AAM	1	1	58	21
Al NP/AAM	2	2.2	70	21
Al NP/AAM	3	3.7	77	21
Black titania	1	1.13	70.9	22
PPy-coated SS meshes	1	0.92	58	23
CNT–silica bilayered material	1	1.32	82	24
<b>CM foam</b>	<b>1</b>	<b>1.458</b>	<b>90.4</b>	<b>This work</b>

**Table S4.** Comparison of solar steam generation performances of various state-of-the-art materials.

Photothermal agent	Solar intensity (kW m <sup>-2</sup> )	Evaporation rate (kg m <sup>-2</sup> h <sup>-1</sup> )	Conversion efficiency (%)	Ref.
VA-GSM	1	1.57	83.5	25
Porous N-doped graphene	1	1.50	80	26
Carbonized mushroom	1	1.475	78	27
RGO-SA-CNT aerogels	1	1.622	83	28
GO film with confined 2D water path	1	1.45	80	29
Flame-treated wood	1	1.05	72	30
CB/GO	1	1.27	87.5	31
Reduced Graphene Oxide Films	1	1.14	89.2	32
Ag/diatomite	1	1.39	92.2	33
<b>CM foam</b>	<b>1</b>	<b>1.458</b>	<b>90.4</b>	<b>This work</b>

## Reference

- 1 N. Gao, Y. Fan, X. Quan, Y. Cai and D. Zhou, *J. Mater. Sci.*, 2016, **51**, 6379-6388.
- 2 D. Kim, D. W. Kim, O. Buyukcakir, M.-K. Kim, K. Polychronopoulou and A. Coskun, *Adv. Funct. Mater.*, 2017, **27**, 1700706.
- 3 K.-G. Zhou, N.-N. Mao, H.-X. Wang, Y. Peng and H.-L. Zhang, *Angew. Chem. Int. Ed.*, 2011, **123**, 11031-11034.
- 4 J. Liu, Z. Zeng, X. Cao, G. Lu, L.-H. Wang, Q.-L. Fan, W. Huang and H. Zhang, *Small*, 2012, **8**, 3517-3522.
- 5 R. Du, X. Gao, Q. Feng, Q. Zhao, P. Li, S. Deng, L. Shi and J. Zhang, *Adv. Mater.*, 2016, **28**, 936-942.
- 6 X. Zhang, Z. Li, K. Liu and L. Jiang, *Adv. Funct. Mater.*, 2013, **23**, 2881-2886.
- 7 S. Lee, B. Kim, S.-H. Kim, E. Kim and J.-H. Jang, *Adv. Funct. Mater.*, DOI: 10.1002/adfm.201702310, 1702310.
- 8 Y. Han, L. Han, L. Zhang and S. Dong, *J. Mater. Chem. A*, 2015, **3**, 14669-14674.
- 9 J.-S. Li, S.-L. Li, Y.-J. Tang, M. Han, Z.-H. Dai, J.-C. Bao and Y.-Q. Lan, *Chem. Commun.*, 2015, **51**, 2710-2713.
- 10 W. Cui, N. Cheng, Q. Liu, C. Ge, A. M. Asiri and X. Sun, *ACS Catal.*, 2014, **4**, 2658-2661.
- 11 Y. Yang, Y. Deng, Z. Tong and C. Wang, *J. Mater. Chem. A*, 2014, **2**, 9994-9999.
- 12 S. Qiu, B. Jiang, X. Zheng, J. Zheng, C. Zhu and M. Wu, *Carbon*, 2015, **84**, 551-559.
- 13 R. Du, Q. Feng, H. Ren, Q. Zhao, X. Gao and J. Zhang, *J. Mater. Chem. A*, 2016, **4**, 938-943.
- 14 Z. Xu, K. Miyazaki and T. Hori, *Adv. Mater. Interfaces*, 2015, **2**, 1500255.
- 15 R. Du, N. Zhang, H. Xu, N. Mao, W. Duan, J. Wang, Q. Zhao, Z. Liu and J. Zhang, *Adv. Mater.*, 2014, **26**, 8053-8058.
- 16 C. Liu, J. Yang, Y. Tang, L. Yin, H. Tang and C. Li, *Colloids Surf., A*, 2015, **468**, 10-16.
- 17 Y. Yang, Z. Tong, T. Ngai and C. Wang, *ACS Appl. Mater. Interfaces*, 2014, **6**, 6351-6360.
- 18 Y. Gao, Y. S. Zhou, W. Xiong, M. Wang, L. Fan, H. Rabiee-Golgir, L. Jiang, W. Hou, X. Huang, L. Jiang, J.-F. Silvain and Y. F. Lu, *ACS Appl. Mater. Interfaces*, 2014, **6**, 5924-5929.
- 19 K. Jayaramulu, K. K. R. Datta, C. Roesler, M. Petr, M. Otyepka, R. Zboril and R. A. Fischer, *Angew. Chem. Int. Ed.*, 2016, **55**, 1178-1182.
- 20 M. Ye, J. Jia, Z. Wu, C. Qian, R. Chen, P. G. O'Brien, W. Sun, Y. Dong and G. A. Ozin, *Adv. Energy Mater.*, 2017, **7**, 1601811.
- 21 L. Zhou, Y. Tan, J. Wang, W. Xu, Y. Yuan, W. Cai, S. Zhu and J. Zhu, *Nat. Photonics*, 2016, **10**, 393-398.
- 22 G. Zhu, J. Xu, W. Zhao and F. Huang, *ACS Appl. Mater. Interfaces*, 2016, **8**, 31716-31721.
- 23 L. Zhang, B. Tang, J. Wu, R. Li and P. Wang, *Adv. Mater.*, 2015, **27**, 4889-4894.
- 24 Y. Wang, L. Zhang and P. Wang, *ACS Sustainable Chem. Eng.*, 2016, **4**, 1223-1230.
- 25 P. Zhang, J. Li, L. Lv, Y. Zhao and L. Qu, *ACS Nano*, 2017, **11**, 5087-5093.
- 26 Y. Ito, Y. Tanabe, J. Han, T. Fujita, K. Tanigaki and M. Chen, *Adv. Mater.*, 2015, **27**, 4302-4307.
- 27 N. Xu, X. Hu, W. Xu, X. Li, L. Zhou, S. Zhu and J. Zhu, *Adv. Mater.*, 2017, 1606762.
- 28 X. Hu, W. Xu, L. Zhou, Y. Tan, Y. Wang, S. Zhu and J. Zhu, *Adv. Mater.*, 2017, **29**, 1604031.
- 29 X. Li, W. Xu, M. Tang, L. Zhou, B. Zhu, S. Zhu and J. Zhu, *Proc. Natl. Acad. Sci. U. S. A.*, 2016, **113**, 13953-13958.
- 30 G. Xue, K. Liu, Q. Chen, P. Yang, J. Li, T. Ding, J. Duan, B. Qi and J. Zhou, *ACS Appl. Mater. Interfaces*, 2017, **9**, 15052-15057.

- 31 Y. Li, T. Gao, Z. Yang, C. Chen, Y. Kuang, J. Song, C. Jia, E. M. Hitz, B. Yang and L. Hu, *Nano Energy*, 2017, **41**, 201-209.
- 32 A. Guo, X. Ming, Y. Fu, G. Wang and X. Wang, *ACS Appl. Mater. Interfaces*, 2017, **9**, 29958-29964.
- 33 J. Fang, Q. Liu, W. Zhang, J. Gu, Y. Su, H. Su, C. Guo and D. Zhang, *J. Mater. Chem. A*, 2017, **5**, 17817-17821.